Chemical Science

ROYAL SOCIETY OF CHEMISTRY

EDGE ARTICLE

View Article Online
View Journal | View Issue



Cite this: *Chem. Sci.*, 2025, **16**, 3571

All publication charges for this article have been paid for by the Royal Society of Chemistry

# Engineering the solid electrolyte interphase for enhancing high-rate cycling and temperature adaptability of lithium-ion batteries†

Zhongming Wang, [a] Zhiyuan He,[a] Zhongsheng Wang,[a] Kecheng Long, [c] Jixu Yang,[a] Shaozhen Huang,[a] Zhibin Wu, [a] Lin Mei *[a] and Libao Chen *[ab]

Received 22nd November 2024
Accepted 15th January 2025

DOI: 10.1039/d4sc07916g

rsc.li/chemical-science

In overcoming the barrier of rapid $Li^+$ transfer in lithium-ion batteries at extreme temperatures, the desolvation process and interfacial charge transport play critical roles. However, tuning the solvation structure and designing a kinetically stable electrode–electrolyte interface to achieve high-rate charging and discharging remain a challenge. Here, a lithium nonafluoro-1-butanesulfonate (NFSALi) additive is introduced to optimize stability and the robust solid electrolyte interface film (SEI), realizing a rapid $Li^+$ transfer process and the structural integrity of electrode materials. The NFSALi-derived thinner, fluorine-rich, and sulfur-containing SEI in nitrile-assisted carbonate electrolytes effectively suppresses the decomposition of valeronitrile solvent during high-rate cycling and wide-temperature operation (−40–55 °C). More importantly, the graphite||$LiNi_{0.5}Co_{0.2}Mn_{0.3}O_2$ pouch cell demonstrates a capacity retention of 66.88% after 200 high-rate cycles with 3C charging and 5C discharging under a high-temperature condition of 55 °C. This work provides significant guidance to develop inorganic-rich interfacial chemistry for lithium-ion batteries under extreme operating conditions.

## 1 Introduction

Lithium-ion batteries (LIBs) receive extensive attention from researchers and institutions worldwide due to their remarkable advantages, such as high energy density, long cycle life, and high safety.[1–3] However, charge transfer across electrode–electrolyte interfaces is one of the primary limitations for high-rate cycling, especially under wide temperature conditions.[4–6] The ionic conductivity of electrolyte and the characteristics of the SEI, along with the occurrence of side reactions, critically affect the efficiency of charge transfer rapidly across multiphase boundaries.[7,8] Additionally, the effect of the operating temperature on the electrolyte further accelerates the degradation of performance in LIBs, including a reduced $Li^+$ migration rate at low temperatures and the recombination of the SEI and cathode electrolyte interface (CEI) at high temperatures.[9,10] Therefore, it is challenging to design an electrolyte to engineer a stable and robust electrode–electrolyte interface, fulfilling the requirements of high-rate cycling and temperature adaptability in LIBs.

Previous studies mainly focused on regulating the solvation structure of $Li^+$ and weakening solvation energy through utilizing multi-component solvents,[11–13] lithium salts,[14,15] and additives.[16–18] However, the influence of electrode–electrolyte interfacial characteristics and the structure on charge transfer remains insufficiently explored.

Nitrile-based solvents have been employed in low-temperature electrolytes due to their low freezing point, high boiling point, and low viscosity characteristics. Lu *et al.*[19] used fluoroacetonitrile as a solvent to effectively construct a ligand channel for high-speed ion conduction, which significantly promotes the migration of $Li^+$, thereby producing an electrolyte with excellent conductivity. The electrolyte can still maintain a high discharge capacity of 0.62 Ah at a low temperature of −65 °C. Our previous work has also investigated the performance of valeronitrile-based electrolytes in LIBs in a wide temperature range from −50 °C to 55 °C.[20] Valeronitrile (VN) is a solvent to effectively enhance the stability of the nitrile electrolyte. In a low-temperature environment of −50 °C, a high discharge retention rate of 65.21% is achieved. At the same time, the electrolyte can still maintain 84.46% capacity after 100 cycles at 1C with 45 °C. However, a notable drawback of nitrile-based solvents in electrolytes is their poor compatibility with anodes, primarily due to the high reactivity of the cyano functional groups.[21] Instability toward low potentials (<0.1 V *vs.* $Li/Li^+$) can also be observed during the reductive decomposition of the nitrile solvent, when exposed to lithium metal or lithiated graphite.[22–24] The high reduction potential of nitrile-based

[a]*State Key Laboratory of Powder Metallurgy, Central South University, Changsha, 410083, P. R. China. E-mail: meilin@csu.edu.cn*

[b]*National Energy Metal Resources and New Materials Key Laboratory, Central South University, Changsha, 410083, P. R. China. E-mail: lbchen@csu.edu.cn*

[c]*School of Materials Science and Engineering, Xiangtan University, Xiangtan, Hunan, 411105, China*

† Electronic supplementary information (ESI) available. See DOI: https://doi.org/10.1039/d4sc07916g

solvents impedes the formation of an effective protective passivation layer on the anode surface, resulting in continuous decomposition of electrolytes and structural degradation of the anode.[25,26] On the other hand, the side reactions catalyzed by nitrile solvents are significantly intensified under high-temperature conditions.[20] This accelerated reactivity not only promotes the rapid degradation of electrode materials but also significantly diminishes the cycle life of LIBs. Therefore, the application of nitrile-based electrolytes in LIBs at wide temperatures remains a significant challenge.

To enable the application of nitrile-based electrolytes in wide-temperature LIBs, extensive efforts have been dedicated to improving the stability of electrolytes through various optimization approaches.[5,27] Huang *et al.*[28] showed that the graphite anode attained rapid charging capabilities across a temperature range of −20 to 60 °C through the optimization of the acetonitrile (AN) to fluoroethylene carbonate (FEC) ratio in electrolyte. Luo *et al.*[29] investigated the impact of various nitrile molecular structures on the cycle stability of the electrolyte. The study indicated that blending isobutyronitrile with carboxylates in a graphite‖$LiCoO_2$ pouch cell achieved excellent cycle stability at −40 °C and 60 °C. Previous research has demonstrated that nitrile-based electrolytes can significantly extend the low-temperature operational range of LIBs; however, cyano functional groups constrain the performance at high temperatures, especially at high-rate current densities.

In this work, lithium nonafluoro-1-butanesulfonate (NFSALi) is employed as an additive in the electrolyte. It promotes the formation of a fluorine- and sulfur-rich SEI on the surface of electrode materials because the lowest unoccupied molecular orbital energy (LUMO) of NFSALi is lower than that of electrolyte solvents. NFSALi preferentially participates in SEI formation, effectively suppressing the decomposition of solvent molecules. The SEI enriched with fluorine and sulfur enhances stability and reduces ionic transfer resistance, thereby facilitating rapid $Li^+$ transportation. An optimized electrolyte based on 1% NFSALi in a nitrile and ester co-solvent electrolyte system exhibits 20C rate capability and wide-temperature performance. The graphite‖$LiNi_{0.5}Co_{0.2}Mn_{0.3}O_2$ (NCM523) pouch cell with NFSALi-containing electrolyte shows excellent high-rate cycle stability at 55 °C.

## 2 Results and discussion

Two electrolyte formulations are prepared. A base electrolyte consisting of 1.2 mol $L^{-1}$ $LiPF_6$ in a mixture of VN, ethyl methyl carbonate (EMC), and FEC with a volume ratio of 3 : 6 : 1, denoted as base. The NFSALi electrolyte is prepared by adding 1.0 wt% NFSALi to the above base electrolyte, denoted as 1% NFSALi.

Density functional theory (DFT) calculations are employed to determine the lowest unoccupied molecular orbital (LUMO) and the highest occupied molecular orbital (HOMO) values of VN, EMC, FEC, and NFSALi (Fig. 1a). Compared to the LUMO energy level of the VN, EMC, and FEC solvents (0.4925, 1.0422, and 0.3129 eV, respectively), the LUMO energy values of NFSALi are −1.6055 eV, indicating its prior reduction compared to other solvent molecules. The probability distribution of electron cloud density of NFSALi is illustrated in Fig. S1,† elucidating the characteristics pertaining to electron repulsion or attraction.[30] It is an indication that NFSALi exhibits a high electron affinity, which can be expected to easily decompose and dominate the SEI formation. Moreover, the bond order of the NFSALi molecule is depicted in Fig. S2,† revealing that the bond order of C–S is 0.701. The lower bond order of C–S promotes decomposition, leading to the formation of sulfur-containing components in

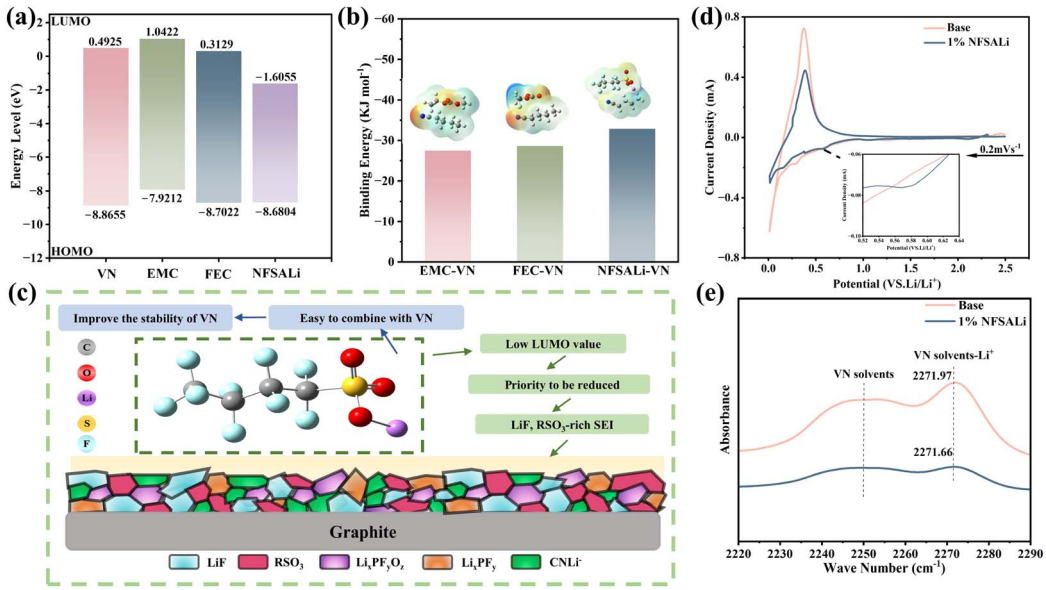


Fig. 1 (a) LUMO and HOMO values of various solvent molecules and NFSALi. (b) Binding energies of solvent molecules and NFSALi with VN. (c) Schematic illustration of the electrochemical performance enhancement of the incorporation of NFSALi. (d) CV of Li‖graphite with different electrolytes at a scanning rate of 0.2 mV $s^{-1}$. (e) Infrared characteristic spectra of cyano functional groups.

the SEI, namely $RSO_3$. The sulfur-containing components have been demonstrated to enhance SEI stability, so as to effectively inhibit the failure of electrode materials and improve the stability and low-temperature performance of the LIBs.[31] Fig. 1b shows the binding energy of EMC, FEC, and NFSALi with VN to be $-27.45$ KJ $mol^{-1}$, $-30.35$ KJ $mol^{-1}$, and $-35.64$ KJ $mol^{-1}$, respectively. This indicates that the addition of NFSALi exhibits strong binding energy with VN, preventing the decomposition of VN solvent molecules.[32] The mechanism of NFSALi improving the performance of LIBs is illustrated in Fig. 1c. The addition of NFSALi enhances the stability of VN and forms an SEI enriched with $RSO_3$ and LiF on the graphite electrodes, which is beneficial to improve the cycling performance and wide-temperature performance of LIBs.

The oxidative stability of the electrolyte is investigated by linear sweep voltammetry (LSV) with a steel foil working electrode, as shown in Fig. S3.† In the base electrolyte, an oxidative current initiated at about 3.6 V at a scan rate of 1 mV $s^{-1}$ and then increased when the potential was swept to 5.25 V, indicating that the base electrolyte suffered from severe oxidative decomposition above 5.25 V. With the addition of 1% NFSALi, the onset of electrolyte oxidation shifted to 4.6 V. There are no peaks of electrolyte decomposition observed between the 5.0 and 5.5 V range, indicating that the NFSALi additive effectively extended the electrochemical stability window. In addition, the position of the reaction peak in the electrolyte was further detected and analyzed using cyclic voltammetry (CV). When comparing the CV results of Li‖graphite batteries with the base electrolyte and the 1% NFSALi electrolyte (Fig. 1d), the latter showed a small reduction peak at about 0.56 V potential during the initial CV cycle. This peak was attributed to the decomposition of NFSALi on the graphite surface, resulting in the formation of the SEI. Infrared spectroscopy was employed to investigate the coordination environment involving lithium ions, solvent molecules, and anions. As shown in Fig. 1e, the peak of the cyano functional groups is at 2250 $cm^{-1}$ and the newly emerged peak after coordination with lithium ions is positioned at about 2271 $cm^{-1}$.[33] In 1% NFSALi electrolytes, the characteristic peak of VN solvents-$Li^+$ has a red shift, indicating that the binding between VN and $Li^+$ is stronger.

The performance of 1.0 Ah graphite‖NCM523 pouch cells with different electrolytes is investigated. Fig. S4† illustrates the cycle performance of cells with different electrolytes at room temperature with 3C charge and 5C discharge (1C = 1.0 A). The pouch cell containing the base electrolyte demonstrated a capacity retention rate of 79.61% after 600 cycles. In contrast,

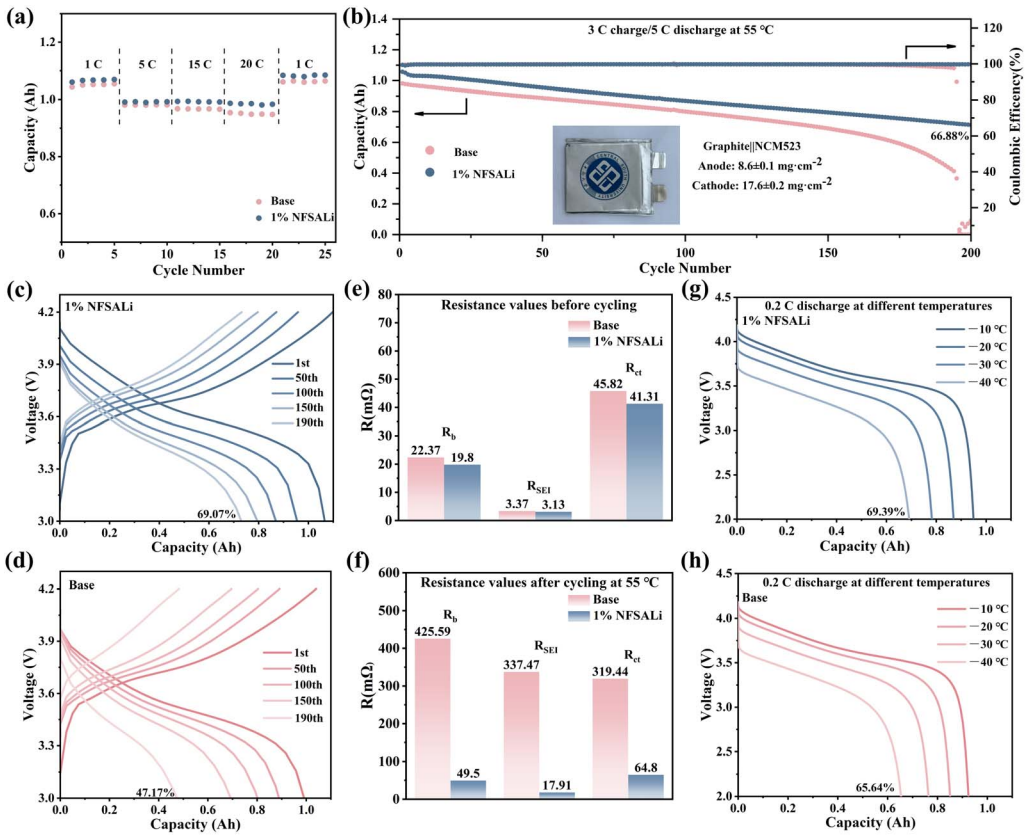


Fig. 2 The performance of graphite‖NCM523 pouch cells with different electrolytes: (a) the rate performance of different electrolytes at room temperature. (b) Cycling performance at a 3C charge/5C discharge rate at 55 °C. (c) The charge–discharge curves of 1% NFSALi electrolytes after different cycles at 55 °C. (d) The charge–discharge curves of the base electrolyte after different cycles at 55 °C (e) The resistance values of each electrolyte before cycling. (f) The resistance values of each electrolyte after 200 cycles at 55 °C. (g) The discharge curves of 1% NFSALi electrolyte with 0.2C at low temperatures. (h) The discharge curves of the base electrolyte with 0.2C at low temperatures.

under the same conditions, the pouch cell with 1% and 2% NFSALi electrolyte exhibited capacity retention rates of 82.20% and 81.56%, respectively. The NFSALi additive can improve the high-rate cycling performance of the LIBs at room temperature due to stable interface physicochemical properties. Fig. 2a illustrates the rate performance of various electrolytes in the pouch cell. At a discharge rate of 20C at room temperature, the discharge capacity of the pouch cell with the 1% NFSLALi electrolyte is 0.98 Ah, while the discharge capacity of the pouch cell with the base electrolyte is only 0.94 Ah. This demonstrates the enhanced ultrahigh-rate discharge performance afforded by the NFSALi additive.

The development of an electrolyte that is capable of simultaneously showing high-temperature stability and high-rate cycling performance remains a challenge. The high-temperature and high-rate cycling performance further prove the advantages of the graphite‖NCM523 pouch cell with 1% NFSALi electrolyte. Fig. 2b shows the cycling performance of the pouch cells with base electrolyte and 1% NFSALi electrolyte in 3C charging and 5C discharging at 55 °C. After 200 cycles, the capacity of the pouch cell with 1% NFSALi electrolyte remains 0.71 Ah with 66.88% capacity retention. In contrast, the pouch cell with the base electrolyte exhibits a significant capacity decay under the same conditions. The electrolyte with 1% NFSALi effectively enhances the cycle stability of the pouch cells at a high-rate and high temperatures. The charge/discharge curves of the pouch cells with different electrolytes (depicted in Fig. 2c and d) reveal that electrochemical polarization significantly expands with an increasing cycle number in the base electrolyte. This expansion is associated with heightened impedance due to severe side reactions. Notably, the presence of the electrolyte with 1% NFSALi mitigates electrochemical polarization, indicating improved interfacial stability in the graphite‖NCM523 pouch cells and fewer side reactions. The dQ/dV curves of various electrolytes with different cycles at 55 °C corroborate this observation (Fig. S5†).

The electrochemical impedance spectroscopy (EIS) test is further carried out to analyze the high-temperature cycling behavior of the pouch cells and investigate the influence mechanism of NFSALi. The impedance of the pouch cell is mainly composed of solid-state electrolyte interface resistance ($R_{SEI}$) generated by electrolyte decomposition, charge transfer impedance ($R_{ct}$), and ohmic internal resistance ($R_b$). As shown in Fig. S6 and S7,† the two semicircle measures at high frequency represent the $R_{SEI}$ and the $R_{ct}$, respectively. Before and after cycling at 55 °C, the obtained data are fitted according to the equivalent circuit in Fig. S6,† and the specific values of $R_b$, $R_{SEI}$, and $R_{ct}$ are obtained, respectively (Fig. 2e and f). Before cycling, the $R_{SEI}$ and $R_{ct}$ of the pouch cell with 1% NFSALi electrolyte are lower than those of the cells with the base electrolyte. After 200 cycles at 55 °C, the $R_b$, $R_{SEI}$, and $R_{ct}$ of the pouch cell with the base electrolyte increased to 425.59 mΩ, 337.47 mΩ, and 319.44 mΩ, respectively. In contrast, the impedance increases of the pouch cell with 1% NFSALi are lower, with 49.5 mΩ, 17.91 mΩ, and 64.8 mΩ, respectively. It can be inferred that the addition of NFSALi alleviates the decomposition of electrolytes and decreases impedance, thereby improving the electrochemical properties of the pouch cell during high-temperature cycling.

To verify the low-temperature performance of the pouch cell with the NFSALi additive, Fig. 2g and h display the discharge capacities of graphite‖NCM523 cells with various electrolytes at 0.2C from −10 °C to −40 °C. This demonstrates that the low-temperature discharge capacity retention rate of the cell with 1% NFSALi electrolyte is higher than that of the cell with base electrolyte. Specifically, at −40 °C with 0.2C, the discharge capacity retention rates for the cell with 1% NFSALi electrolyte and the base electrolyte are 69.39% and 65.64%, respectively. The higher discharge capacity at low temperatures indicates that 1% NFSALi electrolyte exhibited superior transport kinetics.

To analyze the electrode–electrolyte interfacial layer, scanning electron microscopy (SEM) is employed to observe the surficial change of the NCM523 electrodes (Fig. 3a–c). As depicted in Fig. 3a, the NCM523 material is composed of primary particle agglomerates, and the surface of the NCM523 electrode appears smooth, with no observable deposits. The massive decomposition products from electrolyte are observed on the NCM523 electrode in the base electrolyte after 200 cycles at 55 °C (Fig. 3b), resulting in an indistinct interface between NCM523 particles. In contrast, the NCM523 electrode cycled with the 1% NFSALi electrolyte exhibits minor electrolyte decomposition products, and the particle interfaces remain clearly visible, as shown in Fig. 3c. These results suggest that the CEI derived from NFSALi effectively prevents the decomposition of electrolyte on the surface of NCM523 electrodes.

The XRD patterns of the NCM523 electrode before and after 200 cycles at 55 °C are presented in Fig. 3d and e. Notably, all NCM523 electrodes exhibit a well-defined α-$NaFeO_2$ crystal structure, as evidenced by the XRD data.[34] Compared with the original NCM523 electrode, the (003) peak of the cycled NCM523 electrodes shifts to a lower angle, which is due to the lack of lithium ions at the 3a site, resulting in an expansion of the lattice constant *c* due to increased repulsion between oxygen atoms.[18] More prominent shifts are observed for the electrode cycled in base electrolyte compared to the one in 1% NFSALi electrolyte, suggesting that the incorporation of NFSALi can alleviate decomposition of the electrolyte on the NCM electrode surface, thereby reducing the loss of active lithium in the NCM523 electrode. Transmission electron microscopy (TEM) is employed to investigate the thickness of the CEI in different electrolytes after high-temperature cycling. The results revealed that the thickness of the CEI in the base electrolyte and 1% NFSALi electrolyte is 20.47 and 16.67 nm, respectively, after 200 cycles at 55 °C (Fig. S8†). The introduction of NFSALi significantly promotes the formation of a robust and stable CEI, which inhibits the occurrence of side reactions on the surface of the NCM523 electrode. In addition, it significantly slows down the abnormal growth of CEI thickness under high-temperature cycling conditions, thereby greatly improving the cycle stability and durability of nitrile electrolytes in high-temperature environments.

The morphology of graphite electrodes is identified using the SEM (Fig. S9†). The side reaction products are observed on

 

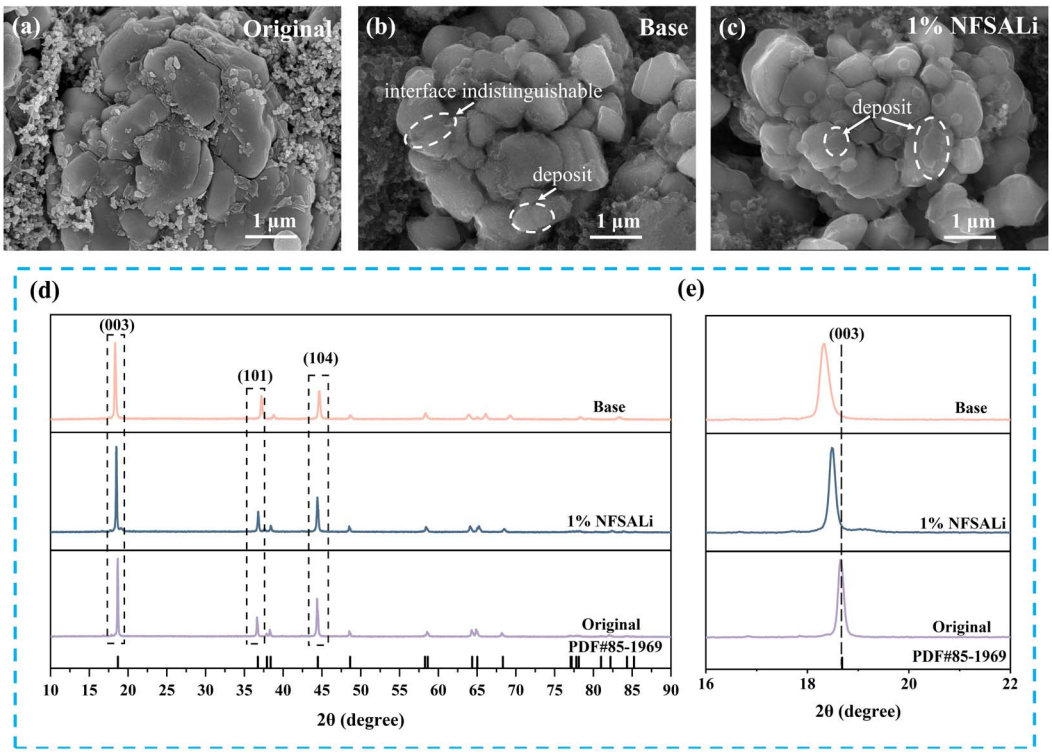


Fig. 3 SEM images of NCM523 electrodes: (a) original, (b) after 200 cycles at 55 °C with base electrolyte, and (c) after 200 cycles at 55 °C with 1% NFSALi electrolyte. (d and e) XRD patterns of NCM523 electrodes before and after 200 cycles at 55 °C with different electrolytes.

the surface of the graphite electrode in the base electrolyte and the 1% NFSALi electrolyte after 200 cycles at 55 °C. The SEM cross-section analysis shows an expansion in the thickness of the graphite electrode after cycling, as shown in Fig. 4a–c. The initial thickness of the graphite electrode is 69.8 μm, while the electrode thickness increases to 120.6 μm after cycling at high temperature in the base electrolyte. The thickness variation of graphite electrodes indicates the formation and growth of the SEI layer and the accumulation of electrolyte decomposition products on the electrode surface, resulting in increased resistance and detachment of active materials. The electrode thickness increases to 86 μm after cycling at a high temperature of the 1% NFSALi electrolyte, demonstrating the thinner SEI formation and fewer side reactions. The TEM reveals the SEI thickness for different electrolytes, as presented in Fig. 4d–g. The results show that the original SEI formed in 1% NFSALi electrolyte is thinner than that in the base electrolyte. After 200 cycles at 55 °C, the SEI thickness formed in the base electrolyte increases to 22.58 nm, whereas the SEI thickness in the 1% NFSALi electrolyte reaches only 14.09 nm. These findings imply that the NFSALi-derived SEI effectively inhibits electrolyte decomposition, providing enhanced electrode stability.

To verify the tendency of transition metal ion dissolution from the cathode after high-temperature and high-rate cycling, Fig. 4h presents the content of transition metal elements in graphite electrodes. In the pouch cell with 1% NFSALi electrolyte, the concentrations of Ni, Co, and Mn are reduced to 16 ppm, 46 ppm, and 66 ppm, respectively. The reduction of transition metal ions proves that the incorporation of NFSALi effectively mitigates the dissolution of Ni, further verifying its role in improving the stability of cathode materials. Fig. 4i presents the Raman spectra of the graphite electrode in its initial state and after cycling at 55 °C. The characteristic peaks located at 1352 $cm^{-1}$ (D-band) and 1583 $cm^{-1}$ (G-band) belong to $sp^3$-type disordered carbon and $sp^2$-type graphitized carbon, respectively. The intensity ratio of the D and G peaks ($I_D/I_G$) reflects the structural integrity of the graphite electrodes.[35] After high-temperature cycling, structural disorder in graphite electrodes increases. However, the addition of NFSALi effectively mitigates this structural degradation. Fig. S10† illustrates the XRD patterns of graphite electrodes in different electrolytes after 200 cycles at 55 °C. Compared to XRD patterns of graphite with the 1% NFSALi electrolyte, the (002) peak of graphite with the base electrolyte shifts to lower diffraction angles, accompanied by an increase in the interlayer spacing ($d_{002}$), resulting from layer structure disruption and fracture. The structural integrity of the graphite with 1% NFSALi electrolyte confirms that the prioritized decomposition of the additive facilitates SEI formation, protecting the electrode structure and enhancing $Li^+$ transport rates.

X-ray Photoelectron Spectroscopy (XPS) is utilized to acquire chemical information on the components of the CEI. The F 1s spectrum of the CEI can be attributed to C–F (689.0 eV), P–F (687.4 eV), and LiF (685.0 eV) bond,[20] as shown in Fig. 5a. The O 1s spectra can be attributed to C–O (533.6 eV), C=O (531.9 eV), and M–O (530 eV, M: transition metal) bonds (Fig. 5b).[36] Notably, the S 2p (Fig. 5c) spectra only appear on the CEI of

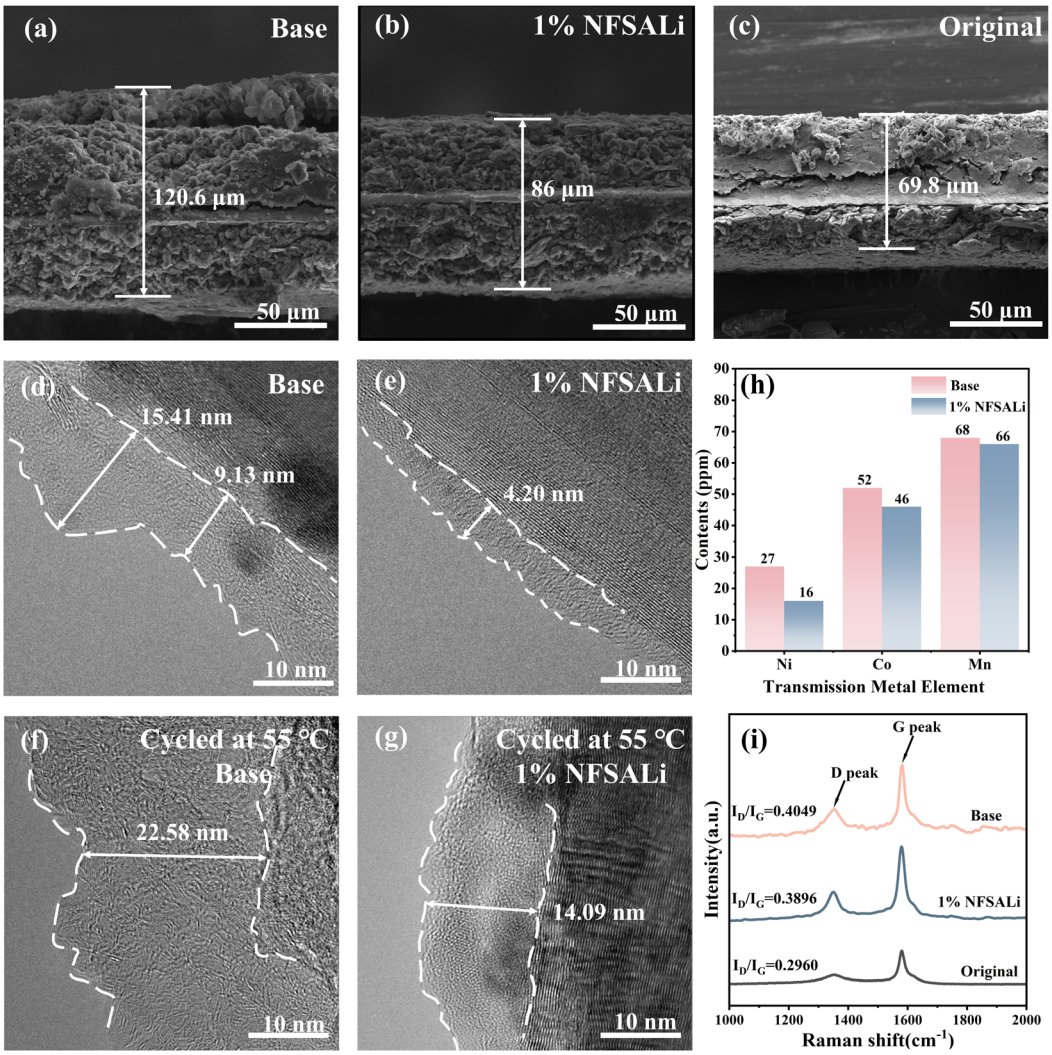


Fig. 4 The cross-sectional SEM images of graphite electrodes: (a) after 200 cycles at 55 °C with base electrolyte, (b) after 200 cycles at 55 °C with 1% NFSALi electrolyte, and (c) original. TEM images of the graphite electrodes: (d) base electrolyte, (e) 1% NFSALi electrolyte, (f) after 200 cycles at 55 °C with base electrolyte and (g) after 200 cycles at 55 °C with 1% NFSALi electrolyte. (h) The content of transition metal elements in graphite electrodes after a high-temperature cycling. (i) The Raman spectrum of the graphite electrodes before and after cycling at 55 °C in base electrolyte and NFSALi-containing electrolyte.

NCM523 electrodes with 1% NFSALi electrolyte, attributing to $RSO_3$ at 170.5 eV and $ROSO_2Li$ at 165.5 eV.[31] For the NCM523 electrode after 200 cycles at 55 °C (Fig. S11 and Table S1†), the highest P–F (74.17%) in F 1s indicates that the base electrolyte decomposes. The S-containing CEI effectively reduces the decomposition of $PF_6^-$ on the surface of NCM523, enhancing the stability of the electrode–electrolyte interface and ultimately improving cycling performance.[31]

The electrochemical stability of graphite electrodes is widely recognized to depend significantly on the complex SEI formed from the electrolyte. In this study, time-of-flight secondary ion mass spectrometry (ToF-SIMS) is performed for the chemical evolution occurring at the surface of the graphite electrodes for both the base electrolyte-derived SEI and 1% NFSALi electrolyte-derived SEI. The $C_2HO^-$ species is attributed to the reduction product of FEC, the $PO_2^-$ species to the reduction of $LiPF_6$,[37] the $SO_3^-$ species to the decomposition of NFSALi, the $CNLi^-$ species to the decomposition of VN,[26] and the $LiF_2^-$ species to the reduction of $LiPF_6$ and FEC, respectively. As the sputtering process continued, all peak signals in the SEI of graphite electrodes reached a steady state. Compared to the base electrolyte-derived SEI, the 1% NFSALi electrolyte-derived SEI exhibited weaker intensities for $C_2HO^-$, $PO_2^-$, and $CNLi^-$ species, while exhibiting stronger intensities for $SO_3^-$ species and $LiF_2^-$ species, as shown in Fig. 6a and b, which is consistent with the DFT results. This observation confirms that the addition of NFSALi effectively reduces the decomposition of $PF_6^-$, FEC, and VN on the graphite electrode surface. At the same time, an inorganic salt-rich SEI ($SO_3^-$ species and $LiF_2^-$ species) formed on the surface of the graphite electrode. The $SO_3^-$ species and $LiF_2^-$ species improve the SEI with flexible and ionic conductivity, resulting in the better cycling performance of the pouch cell with 1% NFSALi electrolyte at a high-rate and high temperature.

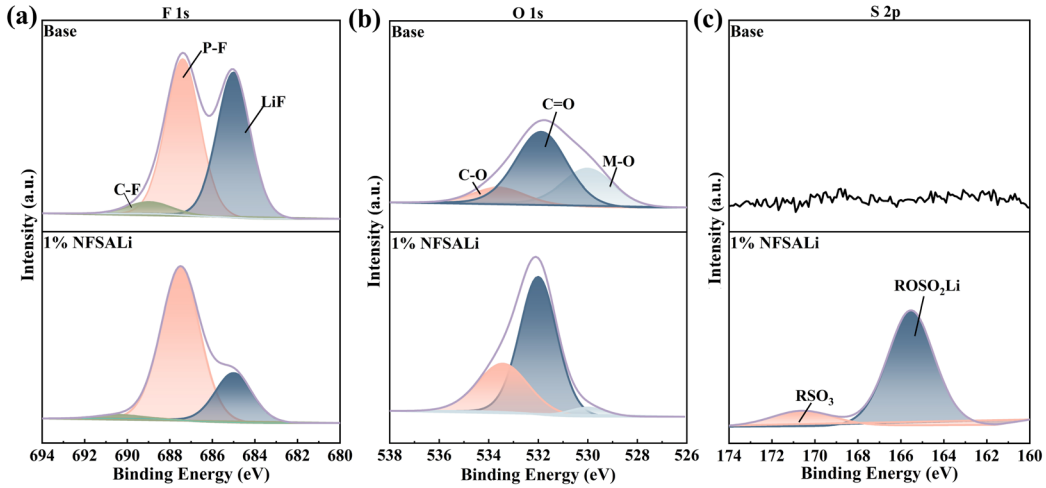


Fig. 5 XPS analysis of the NCM523 electrodes: (a–c) F 1s, O 1s, and S 2p spectra before cycling.

To further investigate the evolution of the SEI during cycling at 55 °C, ToF-SIMS depth profiles are obtained from the graphite electrodes. The 3D rendering of $SO_3^-$ (Fig. 6c–f) reveals the formation of an $SO_3^-$-rich SEI on the SEI of the graphite electrode with 1% NFSALi electrolyte. The decomposition of VN-solvent is suppressed due to the priority formation of the SEI

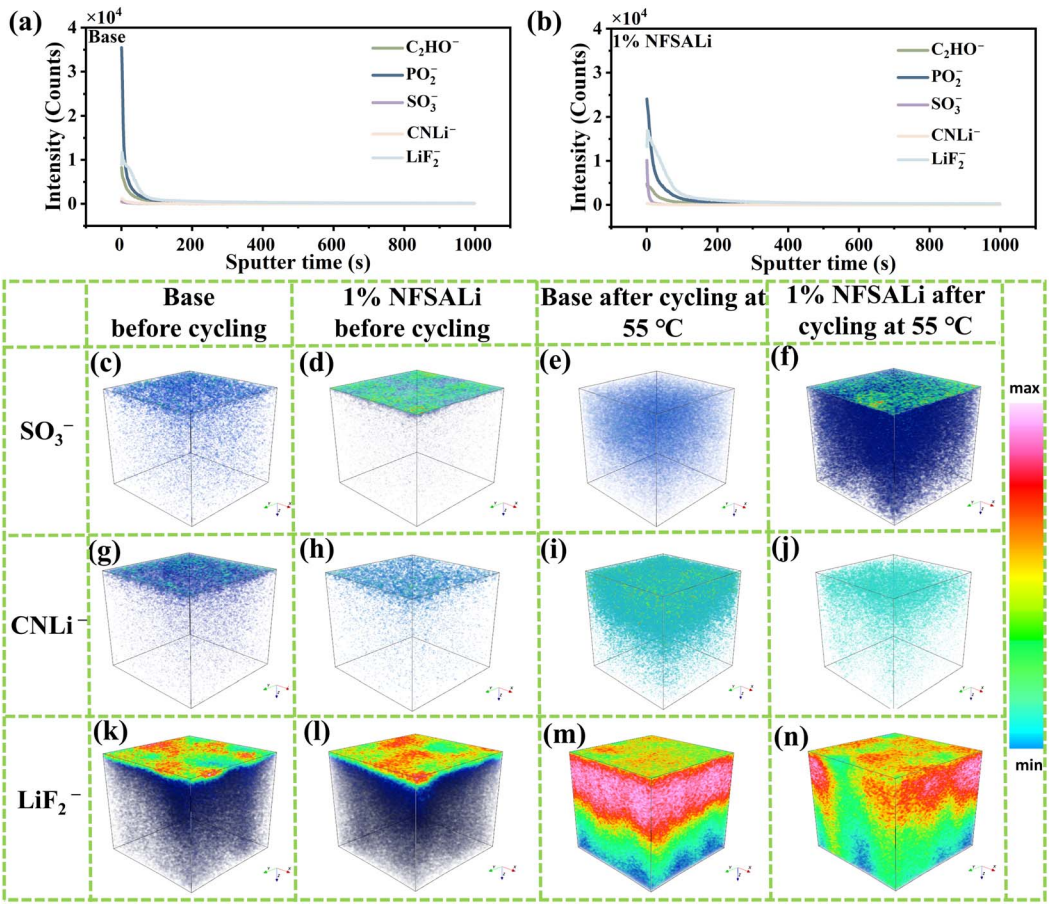


Fig. 6 ToF-SIMS spectra of the graphite electrodes: (a) depth profiles of the ion fragments for the base electrolyte. (b) Depth profiles of the ion fragments for 1% NFSALi electrolyte. (c–f) 3D render of $SO_3^-$: (c) base electrolyte, (d) 1% NFSALi electrolyte, (e) base electrolyte after 200 cycles at 55 °C, and (f) 1% NFSALi electrolyte after 200 cycles at 55 °C. (g–j) 3D render of $CNLi^-$: (g) base electrolyte, (h) 1% NFSALi electrolyte, (i) base electrolyte after 200 cycles at 55 °C, and (j) 1% NFSALi electrolyte after 200 cycles at 55 °C. (k–n) 3D render of $LiF_2^-$: (k) base electrolyte, (l) 1% NFSALi electrolyte, (m) base electrolyte after 200 cycles at 55 °C, and (n) 1% NFSALi electrolyte after 200 cycles at 55 °C.

layer by the NFSALi additive, thus reducing the $CNLi^-$ content in the SEI (Fig. 6g–j). The 3D rendering of $LiF_2^-$ (Fig. 6k–n) shows that the addition of NFSALi promotes the formation of a $LiF_2^-$-rich SEI on the surface of the graphite electrode. However, after 200 cycles at 55 °C, the $LiF_2^-$ content in the NFSALi-derived SEI is lower than that in the basic electrolyte-derived SEI, indicating that NFSALi mitigates the decomposition of FEC during high-temperature cycling. Additionally, the 3D render of $PO_2^-$ (Fig. S11†) further supports the role of NFSALi in reducing $PF_6^-$ decomposition during high-temperature cycling. These results confirm that NFSALi additive-driven formation of an F-rich and S-rich SEI interfacial layer significantly enhances the high-temperature and high-rate performance of LIBs.

# 3 Conclusion

In this study, the incorporation of NFSALi as an additive in VN-based electrolytes is investigated to enhance the performance of LIBs. Electrochemical methods and theoretical calculations reveal that the addition of NFSALi can enhance the stability of VN molecules and preferentially participates in forming an SEI with inorganic salt components ($SO_3^-$ species and $LiF_2^-$ species). The experimental results demonstrate that the capacity retention rate of graphite‖NCM523 pouch cells reaches 82.20% after 600 cycles at a charge rate of 3C and a discharge rate of 5C with the addition of 1% NFSALi to the VN-based electrolyte. Notably, the pouch cells exhibit excellent high-rate cycling stability at high temperatures (55 °C), maintaining a capacity retention rate of 66.88% after 200 cycles. Meantime, the cell with 1% NFSALi electrolyte maintains high discharge capacity retention under extremely low-temperature conditions (−40 °C). In summary, this study not only proposes a novel approach for designing high-performance electrolytes capable of wide-temperature operation but also provides practical insights and a theoretical foundation for the application of nitrile solvents in electrolyte formulations.

# 4 Experimental section

## 4.1 Sample preparation

The lithium salt $LiPF_6$ and electrolyte solvents EMC, FEC, VN, and NFSALi were purchased from the Aladdin reagent network. All the solvents were mixed with molecular sieves to remove trace water. The following electrolytes were prepared in an M. Braun MB-200MOD glovebox filled with Ar gas. The base electrolyte is 1.2 mol $L^{-1}$ $LiPF_6$ in VN/EMC/FEC with a volume ratio of 3 : 6 : 1. The NFSALi electrolyte is 1.2 mol $L^{-1}$ $LiPF_6$ in VN/EMC/FEC with a volume ratio of 3 : 6 : 1 and with 1.0% of the weight ratio of NFSALi added.

## 4.2 Electrochemical measurements

The charge–discharge tests of LIBs were conducted using a Neware CT-ZWJ-4′S-T-1U. The low-temperature and high-temperature electrochemical performances of full cells were measured in a constant temperature test box using a high and low-temperature alternating cycle test chamber. The graphite‖NCM523 pouch cell (no electrolyte) was provided by Hunan Boltpower New Energy Co., Ltd. Graphite and NCM523 were provided by Jilin Juneng Advanced Carbon Materials Co., Ltd and Green Beauty (Wuxi) Energy Materials Co., Ltd, respectively. The anode is composed of 94.5% graphite, 2% SP, 3% LA133, and 0.5% CMC, and the cathode is composed of 94.2% NCM523, 3% SP, 0.6% ECP-600JD, 2.2% PVDF. The mass loading of the anode was 8.6 ± 0.1 mg $cm^2$, while that of the cathode was 17.6 ± 0.2 mg $cm^2$. The electrolyte injection content of each full cell is 4.5 g. After electrolyte injection, the pouch cell was left to stand for 24 hours for formation. The formation process was as follows: 0.05C constant current charging for 260 min and then 0.1C constant current charging for 260 min.

## 4.3 Material characterization

XPS was conducted using Kratos's AXIS SUPRA+ (use Al target material, voltage 15 kV, full spectrum current 5 mA, power 75 W, fine spectrum current 10 mA, and power 150 W). SEM tests were conducted using a Jeol JSM-IT700HR. TEM images were collected using a JEM-F200 from JEOL (shooting voltage: 200 kv and high-resolution magnification: 1.5 million times). To delve deeper into the compositions and structural characteristics of the SEI, ToF-SIMS (ION-TOF TOF.SIMS5) was employed.

## 4.4 Computational details

DFT calculations were performed to optimize the geometries of solvent molecules using the Gaussian 16 package at the B3LYP/6-311g(d,p) level of theory and with Grimme's-D3 (em=gd3bj) dispersion correction. Then, the single point energy was calculated using Grimme's-D3 (em=gd3bj) dispersion correction at the B3LYP/6-311+g(d,p) theoretical level.[38]

# Data availability

The data of this article, including the original Excel file, origin drawing data, theoretical calculation results, *etc.*, can be found in the [Science Data Bank] of [**https://doi.org/10.57760/sciencedb.17306**].

# Author contributions

Zhongming Wang, experimental design, data analysis, data processing, thesis writing. Zhiyuan He, data analysis, data processing. Zhongsheng Wang, data analysis, data processing. Jixu Yang, data analysis. Kecheng Long, data analysis. Shaozhen Huang, data analysis. Zhibin Wu, data analysis. Lin Mei, Libao Chen, data analysis, financial support, review comments reply.

# Conflicts of interest

The authors declare that they have no known competing financial interests or personal relationships that could have appeared to influence the work reported in this paper.

## Acknowledgements

We are thankful for the support from the National Natural Science Foundation of China (92372117), the Innovation-Driven Project of Central South University (Grant No. 2023CXQD024), and the Natural Science Foundation of Hunan Province (Grant No. 2022JJ20068).

## References

1 K. Long, S. Huang, H. Wang, A. Wang, Y. Chen, Z. Liu, Y. Zhang, Z. Wu, W. Wang and L. Chen, *Energy Environ. Sci.*, 2024, **17**, 260–273.
2 Y. Yang, J. Wang, Z. Li, Z. Yang, B. Wang and H. Zhao, *ACS Nano*, 2024, **18**, 7666–7676.
3 S.-Y. Sun, X.-Q. Zhang, Y.-N. Wang, J.-L. Li, Z. Zheng and J.-Q. Huang, *Mater. Today*, 2024, **77**, 39–65.
4 S. Tu, B. Zhang, Y. Zhang, Z. Chen, X. Wang, R. Zhan, Y. Ou, W. Wang, X. Liu, X. Duan, L. Wang and Y. Sun, *Nat. Energy*, 2023, **8**, 1365–1374.
5 S. Lei, Z. Zeng, M. Liu, H. Zhang, S. Cheng and J. Xie, *Nano Energy*, 2022, **98**, 107265.
6 Y.-Y. Wang, Y.-N. Wang, N. Yao, S.-Y. Sun, X.-Q. Ding, C.-X. Bi, Q.-K. Zhang, Z. Zheng, C.-B. Jin, B.-Q. Li, X.-Q. Zhang and J.-Q. Huang, *J. Energy Chem.*, 2024, **95**, 644–650.
7 M. Qin, Z. Zeng, S. Cheng and J. Xie, *Acc. Chem. Res.*, 2024, **57**, 1163–1173.
8 K. Chen, X. Shen, L. Luo, H. Chen, R. Cao, X. Feng, W. Chen, Y. Fang and Y. Cao, *Angew. Chem., Int. Ed.*, 2023, **62**, e202312373.
9 X. Zhuang, S. Zhang, Z. Cui, B. Xie, T. Gong, X. Zhang, J. Li, R. Wu, S. Wang, L. Qiao, T. Liu, S. Dong, G. Xu, L. Huang and G. Cui, *Angew. Chem., Int. Ed.*, 2024, **63**, e202315710.
10 H. Yang, Y. Zhao, T. Qin, H. Pan, S. Feng, Q. Li, X. Wang, X. Yu and H. Li, *ACS Energy Lett.*, 2024, 4475–4484.
11 N. Piao, J. Wang, X. Gao, R. Li, H. Zhang, G. Hu, Z. Sun, X. Fan, H.-M. Cheng and F. Li, *J. Am. Chem. Soc.*, 2024, **146**, 18281–18291.
12 S. Kim, J.-A. Lee, T. K. Lee, K. Baek, J. Kim, B. Kim, J. H. Byun, H.-W. Lee, S. J. Kang, J.-A. Choi, S.-Y. Lee, M.-H. Choi, J.-H. Lee and N.-S. Choi, *Energy Environ. Sci.*, 2023, **16**, 5108–5122.
13 H. Chen, K. Chen, J. Yang, B. Liu, L. Luo, H. Li, L. Chen, A. Zhao, X. Liang, J. Feng, Y. Fang and Y. Cao, *J. Am. Chem. Soc.*, 2024, **146**, 15751–15760.
14 G. Liu, M. Xia, J. Gao, Y. Cheng, M. Wang, W. Hong, Y. Yang and J. Zheng, *ACS Appl. Mater. Interfaces*, 2023, **15**, 3586–3598.
15 H. Chen, K. Chen, L. Luo, X. Liu, Z. Wang, A. Zhao, H. Li, X. Ai, Y. Fang and Y. Cao, *Angew. Chem., Int. Ed.*, 2024, **63**, e202316966.
16 K. Kim, H. Ma, S. Park and N.-S. Choi, *ACS Energy Lett.*, 2020, **5**, 1537–1553.
17 T. Dong, S. Zhang, Z. Ren, L. Huang, G. Xu, T. Liu, S. Wang and G. Cui, *Advanced Science*, 2023, **11**, 2305753.
18 Y. Lin, M. Xu, S. Wu, Y. Tian, Z. Cao, L. Xing and W. Li, *ACS Appl. Mater. Interfaces*, 2018, **10**, 16400–16409.
19 D. Lu, R. Li, M. M. Rahman, P. Yu, L. Lv, S. Yang, Y. Huang, C. Sun, S. Zhang, H. Zhang, J. Zhang, X. Xiao, T. Deng, L. Fan, L. Chen, J. Wang, E. Hu, C. Wang and X. Fan, *Nature*, 2024, **627**, 101–107.
20 Z. Wang, Z. He, Z. Wang, J. Yang, K. Long, Z. Wu, G. Zhou, L. Mei and L. Chen, *Chem. Sci.*, 2024, **15**, 13768–13778.
21 Y. Abu-Lebdeh and I. Davidson, *J. Power Sources*, 2009, **189**, 576–579.
22 C. H. Krause, P. Röring, S. Röser, D. Diddens, J. H. Thienenkamp, I. Cekic-Laskovic, G. Brunklaus and M. Winter, *J. Chem. Phys.*, 2020, **152**, 17.
23 S. Tan, Y. J. Ji, Z. R. Zhang and Y. Yang, *ChemPhysChem*, 2014, **15**, 1956–1969.
24 Y. Yamada, K. Furukawa, K. Sodeyama, K. Kikuchi, M. Yaegashi, Y. Tateyama and A. Yamada, *J. Am. Chem. Soc.*, 2014, **136**, 5039–5046.
25 Y. Abu-Lebdeh and I. Davidson, *J. Electrochem. Soc.*, 2009, **156**, A60–A65.
26 R. Rohan, T.-C. Kuo, J.-H. Lin, Y.-C. Hsu, C.-C. Li and J.-T. Lee, *J. Phys. Chem. C*, 2016, **120**, 6450–6458.
27 A. Fu, J. Lin, Z. Zhang, C. Xu, Y. Zou, C. Liu, P. Yan, D.-Y. Wu, Y. Yang and J. Zheng, *ACS Energy Lett.*, 2022, **7**, 1364–1373.
28 X. Huang, R. Li, C. Sun, H. Zhang, S. Zhang, L. Lv, Y. Huang, L. Fan, L. Chen, M. Noked and X. Fan, *ACS Energy Lett.*, 2022, **7**, 3947–3957.
29 L. Luo, K. Chen, H. Chen, H. Li, R. Cao, X. Feng, W. Chen, Y. Fang and Y. Cao, *Adv. Mater.*, 2024, **36**, 2308881.
30 J. Zhou, B. Hao, M. Peng, L. Zhang, H. Ji, J. Liu, W. Ling, C. Yan and T. Qian, *Adv. Energy Mater.*, 2023, **13**, 2204174.
31 H. Zhao, S. Hu, Y. Fan, Q. Wang, J. Li, M. Yuan, X. Ma, J. Wang, H. Shao and Y. Deng, *Energy Storage Mater.*, 2024, **65**, 103151.
32 K. Guo, C. Zhu, H. Wang, S. Qi, J. Huang, D. Wu and J. Ma, *Adv. Energy Mater.*, 2023, **13**, 2204272.
33 T. Qin, H. Yang, L. Wang, W. Xue, N. Yao, Q. Li, X. Chen, X. Yang, X. Yu, Q. Zhang and H. Li, *Angew. Chem., Int. Ed.*, 2024, **63**, e202408902.
34 C. Liang, L. Jiang, Z. Wei, W. Zhang, Q. Wang and J. Sun, *J. Energy Chem.*, 2022, **65**, 424–432.
35 P. Xiao, Z. Wang, K. Long, J. Yang, X. Liu, C. Ling, L. Chen and L. Mei, *RSC Adv.*, 2024, **14**, 13277–13285.
36 Z. Chen, L. Zhang, X. Wu, K. Song, B. Ren, T. Li and S. Zhang, *J. Power Sources*, 2019, **439**, 227056.
37 J. Y. Liang, Y. Zhang, S. Xin, S. J. Tan, X. H. Meng, W. P. Wang, J. L. Shi, Z. B. Wang, F. Wang, L. J. Wan and Y. G. Guo, *Angew. Chem., Int. Ed.*, 2023, **62**, e202300384.
38 E. R. Johnson, S. Keinan, P. Mori-Sánchez, J. Contreras-García, A. J. Cohen and W. Yang, *J. Am. Chem. Soc.*, 2010, **132**, 6498–6506.